

Anthracene–Triphenylamine-Based Platinum(II) Metallacages as Synthetic Light-Harvesting Assembly

Yanrong Li,* Sreehari Surendran Rajasree, Ga Young Lee, Jierui Yu, Jian-Hong Tang, Ruidong Ni, Guigen Li, Kendall. N. Houk, Pravas Deria,* and Peter J. Stang*



Cite This: *J. Am. Chem. Soc.* 2021, 143, 2908–2919



Read Online

ACCESS |



Metrics & More

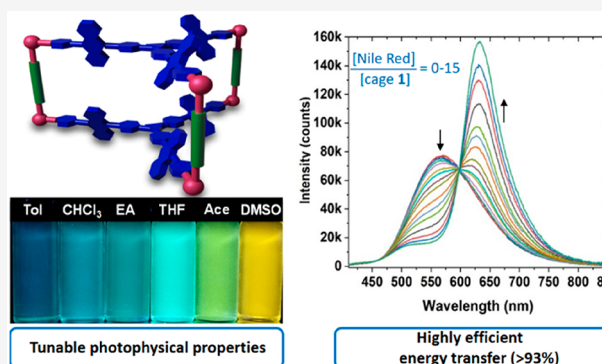


Article Recommendations



Supporting Information

ABSTRACT: Two trigonal prismatic metallacages **1** and **2** bearing triphenylamine and anthracene moieties are designed and synthesized to fabricate artificial light-harvesting systems (LHSs). These two cages are prepared via the coordination-driven self-assembly of two anthracene–triphenylamine-based tripyridyl ligand **3**, three dicarboxylates, and six 90° Pt(II) acceptors. The design of the anthracene–triphenylamine chromophore makes possible the tunable excited-state property (like the emissive transition energy and lifetime) as a function of the solvent polarity, temperature, and concentration. The synergistic photophysical footprint of these metallacages, defined by their high absorptivity and emission quantum yield (QY) relative to the free ligand **3**, signifies them as a superior light sensitizer component in an LHS. In the presence of the fluorescent dye Nile Red (NR) as an energy acceptor, the metallacages display efficient (>93%) excited energy transfer to NR through an apparent static quenching mechanism in viscous dimethyl sulfoxide solvent.



INTRODUCTION

Light harvesting is a key process for photonic energy conservation. In the natural photosynthetic apparatus, the antenna pigments are precisely assembled within the ring of light-harvesting complexes (LHCs).¹ Such arrangement of chlorophylls (and carotenoids) provides highly synergistic excited-state properties like strong photon absorptivity and modular emission energy, where various energy-wasting excited-state decay processes are systematically suppressed. These features enable excited energy transfer to neighboring LHC and eventually to the reaction center (RC) with remarkable efficiency. Inspired by this extraordinary structure and functionality, many artificial light-harvesting systems (LHSs) were developed,^{2–6} among which entirely synthetic supramolecular pigment assembly signifies a novel approach.^{7–10} Such techniques can provide easier access to (a) modular interchromophoric positioning to control the photophysical properties like high photon absorptivity and suppressed unproductive excited-state recombination and (b) scalable synthesis for applications.

Coordination-chemistry-driven self-assembly offers a straightforward synthetic approach for the construction of diverse supramolecular coordination complexes (SCCs), ranging from two-dimensional (2D) metallacycles to three-dimensional (3D) metallacages.^{11–19} With precisely controlled inner cavities, various 3D metallacages have proven to be useful in guest encapsulation, catalysis, sensors, bioimaging

agents, and so on.^{20–24} While tetraphenylethylene (TPE)-based tetragonal prismatic Pt(II) metallacages have been developed as highly emissive SCCs^{25–29} that can be exploited as a light-harvesting system,³⁰ we wanted to integrate photophysical tunability in these metallacages. For this, we adopted ligand design based on a triphenylamine (TPA) as an electron-rich, propeller-shaped C₃ symmetric central component—with the expectation that the resulting pyridine-appended ligand and the corresponding cage-assemblies could provide external stimuli-responsive photophysics. While TPA-based ligand has been used in the construction of hexagonal Pt(II) metallacycles,³¹ we targeted trigonal prismatic Pt(II) cages given that such organic fluorophores are rare and can potentially open up further exploration of new cages with tunable size and photophysical properties for LHSs. With impressive photophysical properties, we integrated the blue-emitting anthracene component^{32,33} within our pyridine-appended TPA-based macromolecular ligand design for stimuli-responsive fluorescent 3D metallacages.^{34,35} Herein, we describe the preparation of two trigonal prismatic

Received: December 11, 2020

Published: February 12, 2021



Scheme 1. Formation of Metallacages Bearing Triphenylamine and Anthracene Moieties via Coordination-Driven Self-Assembly

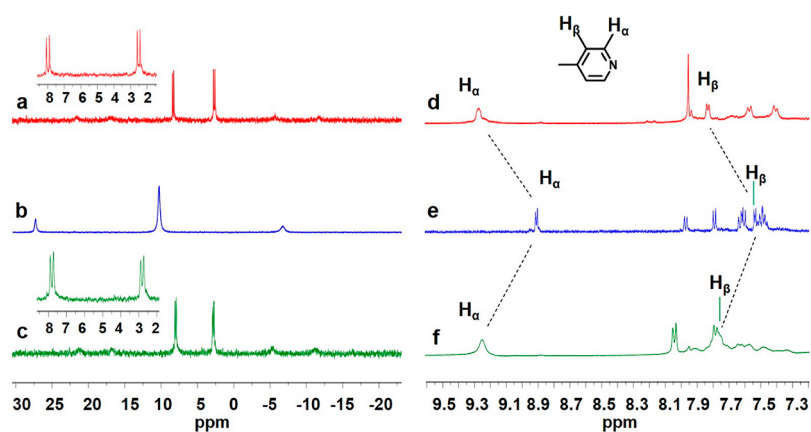
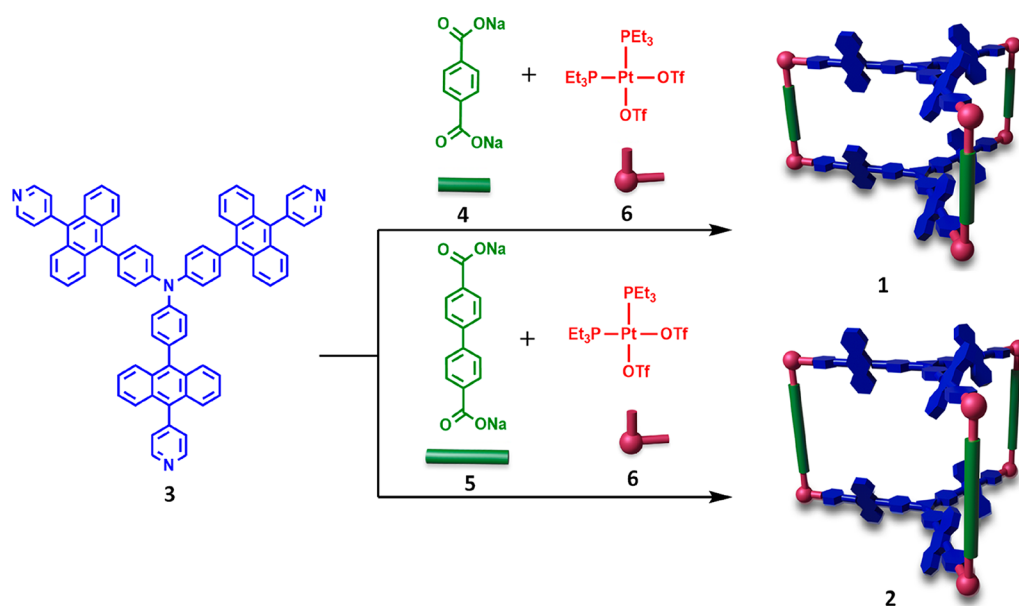


Figure 1. ^{31}P $\{^1\text{H}\}$ NMR spectra of cage 1 (a), ligand 6 (b), and cage 2 (c) (121 MHz, acetone- d_6 , 298 K). Partial ^1H NMR spectra of cage 1 (d), ligand 3 (e), and cage 2 (f) (500 MHz, acetone- d_6 , 298 K).

platinum(II) cages with anthracene and triphenylamine moieties. The cages display synergistic, yet tunable photo-physical properties as a function of solvent polarity, temperature, and concentrations. Notably, these supramolecular constructs display superior light-harvesting behavior with a strong light absorptivity and emission quantum yield (QY) which can efficiently transfer the excited-energy to a suitable acceptor like Nile Red (NR) in dimethyl sulfoxide solution.

RESULTS AND DISCUSSION

Cage Preparation and Characterization. The organic ligand 3 was synthesized by a Pd-catalyzed Suzuki–Miyaura cross-coupling reaction between 4-(10-bromoanthracen-9-yl)pyridine and (nitrilotris(benzene-4,1-diyl))triboronic acid (Schemes S1–S4 in the Supporting Information).³⁶ Metallacages 1 and 2 were prepared via a three-component coordination-driven self-assembly strategy (Scheme 1).^{37,38} Ligand 3, one of the dicarboxylates (4 or 5), and 90° Pt(II) (6) were mixed in a molar ratio of 2:3:6 in a mixture of acetone and water (4/1, v/v). The mixture was stirred for 12 h at 35°C , and then the solvents were removed. Acetone was

added to the dried residues, followed by the addition of diethyl ether. The resulting precipitates were collected by centrifugation, and the desired metallacages were obtained in over 90% yields. These metallacages exhibit better solubility in acetone compared to the pristine ligands. The structures of these cages are established by multinuclear NMR (^1H NMR and ^{31}P $\{^1\text{H}\}$ NMR), correlation spectroscopy (COSY) NMR, and electrospray ionization time-of-flight mass spectroscopy (ESI-TOF-MS). While the ^{31}P $\{^1\text{H}\}$ NMR spectrum of 90° Pt(II) (6) exhibits a sharp singlet with concomitant ^{195}Pt satellites (Figure 1b), the ^{31}P $\{^1\text{H}\}$ NMR spectra of cage 1 and cage 2 (Figures 1a and 1c) exhibit two doublets of approximately equal intensity with concomitant ^{195}Pt satellites at 8.02 and 2.46 ppm for 1 and 7.92 and 2.70 ppm for 2. They are corresponding to two distinct phosphorus environments, indicating the heteroligation of the Pt(II) center on 1 or 2 with one pyridyl and one carboxylate moiety. In the ^1H NMR spectra of 1, H_α shifted downfield from 8.90 to 9.28 ppm and H_β shifted downfield from 7.54 to 7.84 ppm compared to the free pyridine of ligand 3, indicating the loss of electron density of the pyridyl unit upon coordination (Figures 1d and 1e).

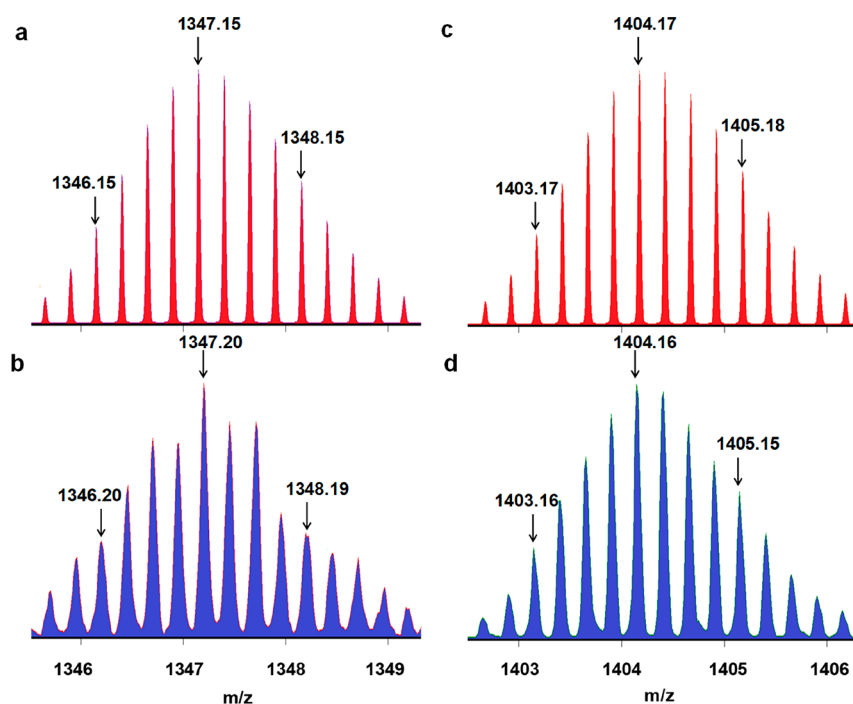


Figure 2. Calculated (red) and experimental (blue) ESI-TOF-MS spectra of metallacage 1 $[M - 4OTf]^{4+}$ (a, b) and metallacage 2 $[M - 4OTf]^{4+}$ (c, d).

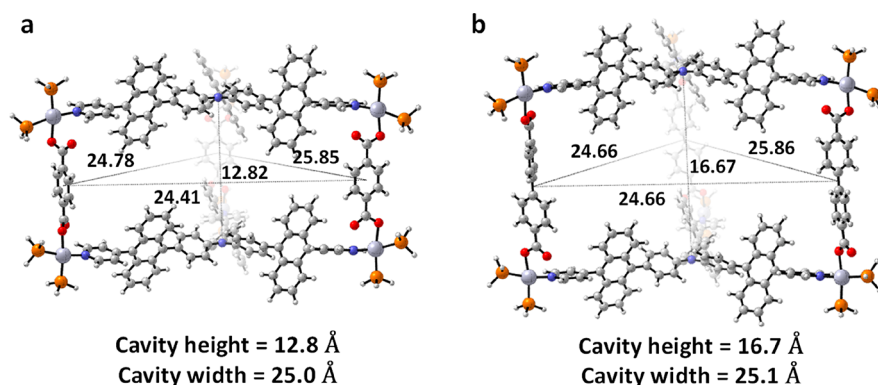


Figure 3. Computational modeling and dimensions of (a) cage 1 and (b) cage 2. Structures were optimized with the PM6 semiempirical method.

Similar downfield shifts are also observed for the pyridyl protons H_α (from 8.90 to 9.26 ppm) and H_β (from 7.54 to 7.76 ppm) of **2** (Figures 1e and 1f). The assignments of these protons are further supported by $^1H-^1H$ COSY NMR analysis (Figures S6, S8, and S13). In Figures S11 and S16, DOSY NMR experiments of **1** and **2** display a single set of signals, indicating the formation of a single product. The measured diffusion coefficients for **1** and **2** are 5.61×10^{-10} and 4.34×10^{-10} m^2/s , respectively. Electrospray ionization time-of-flight mass spectra (ESI-TOF-MS) show isotopically resolved peaks at $m/z = 1347.20$ and 1404.16 , which correspond to the $[M - 4OTf]^{4+}$ species of metallacages **1** and **2**, respectively, and agree well with their calculated theoretical distributions, further supporting the stoichiometric formation of these discrete metallacages (Figure 2).^{39–41} Additionally, the ESI-TOF-MS results of $[M - 3OTf]^{3+}$ signals of the two metallacages also match well with the calculated values (Figures S10 and S15).

The structures and dimensions of metallacages **1** and **2** were simulated by using PM6 computations. Both cages show a triangular prism 3D structure with two planar triphenylamine

faces, three dicarboxylate pillars, and six $\sim 90^\circ$ Pt vertices. The height (N–N distance) and the width (Ph–Ph centroid distance) of cage **1** are 12.8 and 25.0 Å, respectively (Figure 3a). For cage **2**, the height and the width are 16.7 and 25.1 Å, respectively (Figure 3b). This shows that the cavity heights can be tuned depending on the length of the dicarboxylate ligands. In fact, the anthracene moieties are slanted and hinder the cavities' opening, making the accessible width of these cavities smaller and more preorganized.

Photophysical Studies. Excited-State Properties. The photophysical properties of two metallacages **1** and **2**, as well as ligand **3**, were investigated by UV–vis absorption and fluorescence spectroscopy (Figure 4). The UV/vis absorption spectra of ligand **3**, cage **1**, and cage **2** collected in acetone solvent show characteristic $\pi-\pi^*$ -dominated transitions peaking at 355, 378, and 395 nm (Figure 4a).⁴² Nevertheless, the metallacages manifested higher absorptivity than the ligand **3** ($\times 2$) without any significant spectral shift. (A nominal red-shift in the order of a few nanometers can be discerned for **1** and **2** relative to **3**.) These data suggest that such C_3 symmetric

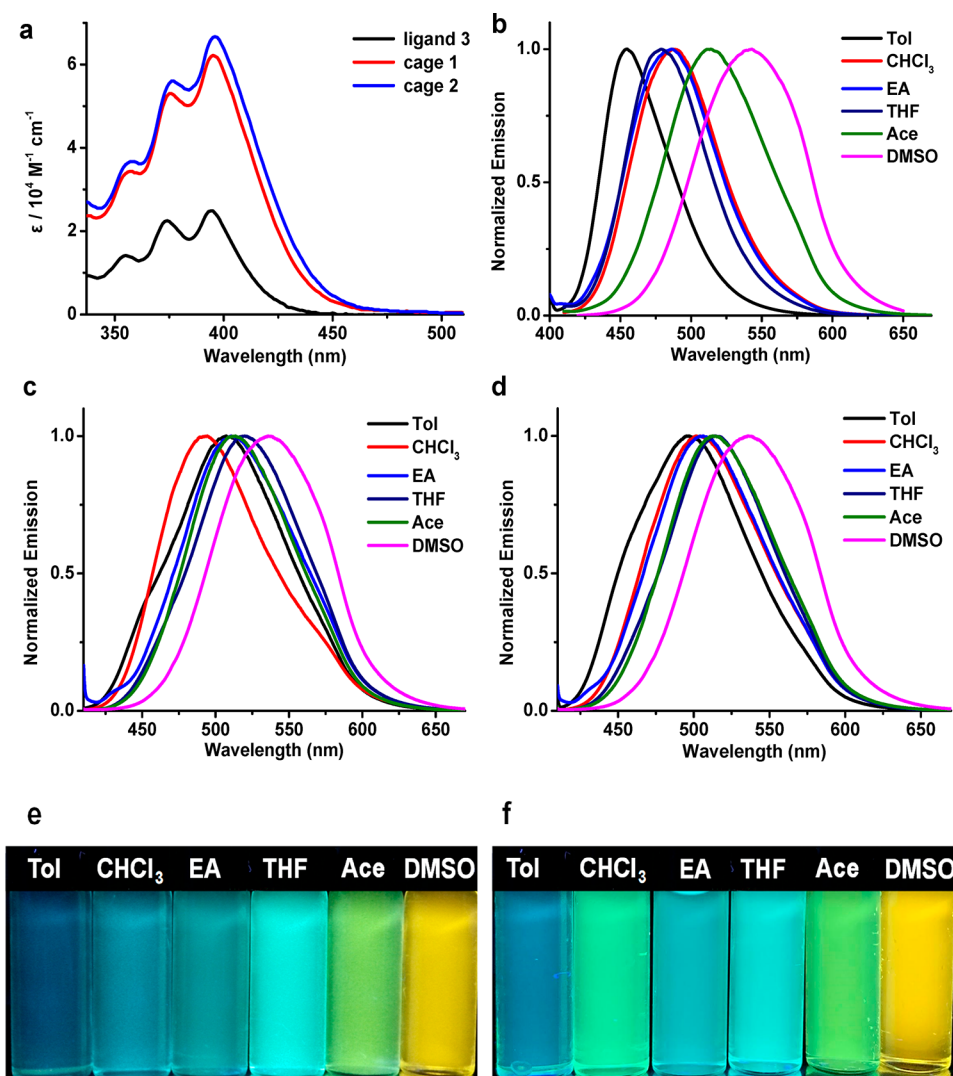


Figure 4. UV/vis absorption spectra of **3**, **1** and **2** (a) in acetone and the normalized fluorescence spectra of ligand **3** (b, $c = 2.0 \times 10^{-6}$ M), metallacage **1** (c, $c = 2.0 \times 10^{-6}$ M), and metallacage **2** (d, $c = 2.0 \times 10^{-6}$ M) in different solvents ($\lambda_{\text{ex}} = 395$ nm). Photographs of metallacages **1** (e) and **2** (f) in different solvents on excitation at 365 nm with an ultraviolet lamp at 298 K ($c = 2.0 \times 10^{-6}$ M). Tol, toluene; EA, ethyl acetate; THF, tetrahydrofuran; Ace, acetone; DMSO, dimethyl sulfoxide.

chromophores, arranged in a trigonal prismatic cage (fixed at 12–16 Å apart), may not produce a strongly coupled system in the absorptive excited state. Ligand **3** shows essentially unchanged absorptive spectral envelope in common solvents of varying polarities, such as toluene, chloroform, ethyl acetate, tetrahydrofuran, and dimethyl sulfoxide (Figure S18), suggesting that the excited state accessed through the vertical electronic excitation is similar to the ground state, featuring a nonpolar aromatic structure. A slight band broadening (particularly at the low-energy side of the lowest energy transition at 395 nm) can be observed for cages **1** and **2**, especially in less polar solvents (Figures S19 and S20). This solvent-dependent change in the absorption spectral envelope, at the red side of the lowest energy transition, may not be entirely stemming from common aggregation-induced process known for such macromolecular compounds.⁴³ Instead, this could be stemming from weak low-energy transitions involving the ligand and 90° Pt(II) node in the cage assembly.⁴⁴ Interestingly, the emission spectral envelop for ligand **3** show a substantial solvatochromism: with an increase in solvent polarity, the emissive spectral peak gradually shifts to the

lower energy (by ~ 3600 cm^{-1} going from toluene to DMSO solvents). As shown in Figure 4b, ligand **3** displays an emission maximum ($\lambda_{\text{em,max}}$) at 454 nm in toluene, which gradually shifts to 543 nm in dimethyl sulfoxide. Such a wide bathochromic shift can be displayed by a change in the emission colors, varying from dark blue to yellow, under a 365 nm ultraviolet lamp (Figure S21). This solvatochromic behavior is mostly maintained in cages **1** and **2** (Figures 4c and 4d), where the degree of the bathochromic shift is smaller than that of **3** with only a blue to yellow color change (Figures 4e and 4f). This is because the emission spectra of the cages are already red-shifted (compared to ligand **3**) to start with in less polar solvent, possibly due to a bit restricted anthracene rotation.

Nature of the Excited States. On the basis of these solvent-dependent absorption and emission spectroscopic data, we believe that the excited state accessed via a direct electronic excitation features an aromatic conformation consisting of a nonplanar amine moiety and anthracene units with a wide range of rotational populations thermally accessible at room temperature. However, this nonpolar aromatic excited state is coupled with a polar quinoidal state, which is facilitated by the

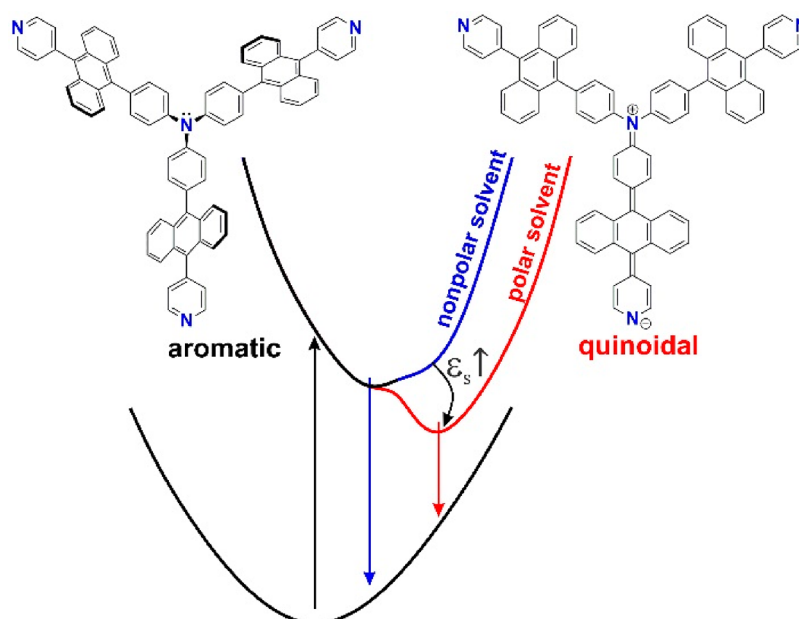


Figure 5. Potential energy surface of an aromatic and quinoidal excited state of 3.

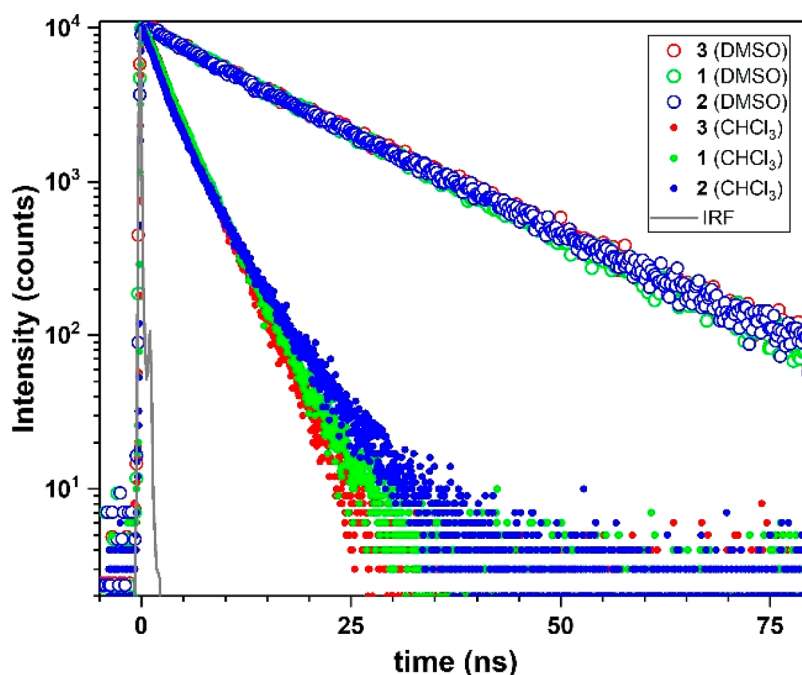


Figure 6. Transient emissive decay profiles for 3, 1, and 2 in DMSO ($\lambda_{\text{probe}} = 540$ nm) and CHCl_3 ($\lambda_{\text{probe}} = 470, 485,$ and 510 nm, respectively) solvents. Experimental conditions: $c = 2.0 \times 10^{-6}$ M, $\lambda_{\text{ex}} = 403$ nm, RT.

9,10-connected anthracene moiety resulting in two complete benzene leading to a planar conformation (Figure 5). The energy of this polar quinoidal state depends on solvent polarity. These two excited states are strongly coupled with efficient intersystem crossing ($k \gtrsim 10^{11} \text{ s}^{-1}$; as no rise event was seen in transient emission profile, Figure 6). This assignment can be supported by thermally arresting the rotation of the anthracene moiety in nonpolar solvent encouraging it to adopt a planar conformer: a systematic red-shift in the emissive peak was observed upon lowering the temperature of 3 (as well as 1 and 2) in nonpolar chloroform solvent (Figure S28).

Table 1 summarizes emission QY and lifetime data. Relative to the ligand 3, cages 1 and 2 show comparable emission QY, particularly in nonpolar CHCl_3 solvent. Interestingly, emission from the polar quinoidal state, stabilized in high dielectric DMSO solvent, did not lead to any significant loss in QY as can be expected from the bandgap law. This planar state is structurally different (Figure 5) than the initially prepared aromatic excited state; thus, the radiative decay from this polar excited state in DMSO is slow ($\tau = 16$ ns) compared to that observed from an aromatic excited state in nonpolar chloroform solvent (3 ns). Overall, with improved (or comparable) absorptivity and emission QY, along with a prolonged excited-

Table 1. Emission QY and Lifetime for the 3, 1, and 2 in Two Different Solvents

| comp (solvent) | QY/% | τ /ns (amplitude) |
|------------------------|-------------------|------------------------|
| 3 (DMSO) | 71 ^a | 15.8 (100) |
| 1 (DMSO) | 60 ^a | 16.2 (100) |
| 2 (DMSO) | 65 ^a | 79 ^b |
| 3 (CHCl ₃) | 72 ^b | 3.3 (100) |
| 1 (CHCl ₃) | 68 ^b | 3.3 (86), 6.4 (14) |
| 2 (CHCl ₃) | 67.8 ^b | 2.4 (55), 5.4 (45) |

^a3 μ M. ^b0.3 μ M.

state lifetime, these cage compounds signify good photosensitizers.

Ligand 3, cage 1, and cage 2 also display a concentration-dependent emissive behavior where the transition energy and QY change as a function of concentration. Emission spectra collected in acetone solvent at different concentrations (7.8×10^{-7} – 4.8×10^{-5} M) are summarized in Figures S22, S24, and S26. For example, after reaching 2.4×10^{-5} M, 3 displays a decrease in QY with a further increase in concentration. This is due to the increased nonradiative decay of the excited states through aromatic–aromatic interactions at high concentrations.⁴⁵ A similar phenomenon is also observed in the emissions of 1 and 2. However, the emission bands of 1 and

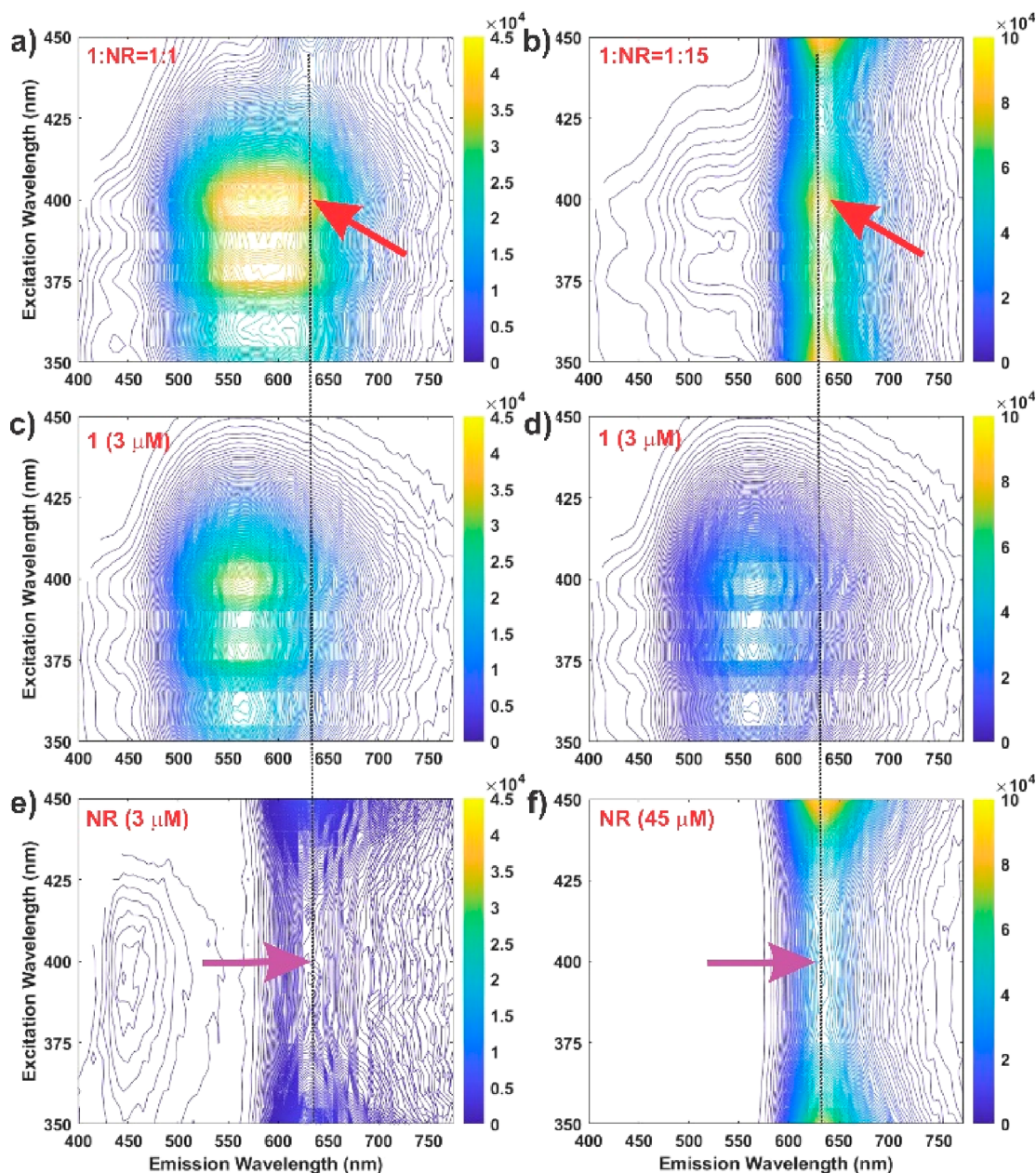


Figure 7. Excitation–emission mapping spectra highlighting EnT process in DMSO solvent involving 1 (3 μ M) at two different NR concentrations: (a) 3 μ M NR and (b) 45 μ M NR. Mapping spectra for pristine (c, d) cage 1 of 3 μ M and (e, f) NR of 3 and 45 μ M solutions in DMSO solvent are provided for comparison (the vertical dashed lines are to guide the NR emission wavelength). The red arrows in panels a and b highlight enhanced emission intensity of NR at 400 nm due to $1^* \rightarrow$ NR EnT compared to its pristine state as shown by the purple arrows in panels e and f.

2 are red-shifted ($\Delta\nu \approx 1600 \text{ cm}^{-1}$) after they reach a concentration of 3.0×10^{-6} and $6.0 \times 10^{-6} \text{ M}$, respectively. This shift is not observed in 3, suggesting that metallacages are quicker to aggregate than the ligand 3.

Excited-State Energy Transfer. With several advantageous photophysical properties, we wanted to test whether the cage compound can transfer its excited state energy to an acceptor and, if so, how the EnT matrices will fare in compounds 1 and 2. In singlet manifold, the Förster resonance energy transfer (FRET) rate constant ($k_{\text{FRET}} = 2\pi J^2 \Theta / \hbar$) depends on the overlap integral Θ (eV^{-1}) between the area-normalized donor fluorescence and acceptor absorption bands and donor–acceptor interchromophoric electronic coupling J (eV^{-1}).^{46–50} The requirement for high Θ stems from Fermi's golden rule to conserve energy and may not involve absorption of an emitted photon by the acceptor, and J can be modulated by the donor–acceptor distance and orientation (i.e., the relative position of the chromophores).^{46–50} With these criteria in mind, we chose Nile Red (NR) with maximum spectral overlap (the transition maximum: $\lambda_{\text{abs(NR)}} \approx \lambda_{\text{em(cage 1 or 2)}} \sim 554 \text{ nm}$) as a candidate acceptor to study EnT in DMSO solvent.⁵¹ Excitation–emission mapping spectra of $3 \mu\text{M}$ cage 1 in the presence of 3 and $45 \mu\text{M}$ NR are shown in Figure 7a,b (see Figure S29 for the corresponding experiment with cage 2). The data highlight, for the equal mixture, an increase in NR emission at 400 nm excitation where it originally does not emit well (Figure 7e). It is also clear that a significant amount of cage 1 emission exists for this equal mixture. The NR emission at 400 nm excitation can be more clearly observed in the excitation–emission mapping spectra for the 1:15 (i.e., in the presence of large excess of NR) mixture (Figure 7b; shown by the red arrows) as emission from cage 1 is nearly quenched. Excitation–emission mapping spectra collected over a wider excitation wavelength range (Figure S30) suggests that the components (cage and NR) can also be independently excited in their mixtures. To ensure that the enhanced NR emission intensity is stemming from the $1^* \rightarrow \text{NR}$ EnT process, we analyzed the excitation profiles: Figure 8a shows that the emission probed at 635 nm (at λ_{max} for NR emission) has a contribution from the cage 1 excitation at around the 400 nm region. Given that the tail of the cage 1 emission also extends to the 635 nm region (Figure 7c,d), it is obvious that emission probed at 635 nm should have some contribution from cage 1 excitation. To clarify this point, we extracted the emission profiles contribution of the NR component (using Voigt deconvolution profile; *vide infra*); data presented in Figure 8b highlight a more than 30-fold increase in NR emission intensity in an equal mixture with the cage 1 compared to the pristine ($3 \mu\text{M}$) NR due to the underlying $1^* \rightarrow \text{NR}$ EnT process at 400 nm excitation (see Figure S31 for the corresponding experiment with cage 2).

To gain insight into the $1^* \rightarrow \text{NR}$ EnT mechanism, we collected transient emission profiles for the cage compounds in the presence of different concentrations of NR. Figure 9 highlights the transient decay profiles of 1 in pristine and in the presence of NR (see Figure S32 for cage 2), and the fitting data suggest the emission decay time for 1^* remains unchanged even with a large excess of NR (relative to its pristine solution). Given that the presence of NR only manifests a diminished QY without impacting the emissive lifetime, we anticipate that the EnT event occurs through a static quenching. Such a mechanism does not involve collision-mediated quenching of 1^* with the NR but instead through

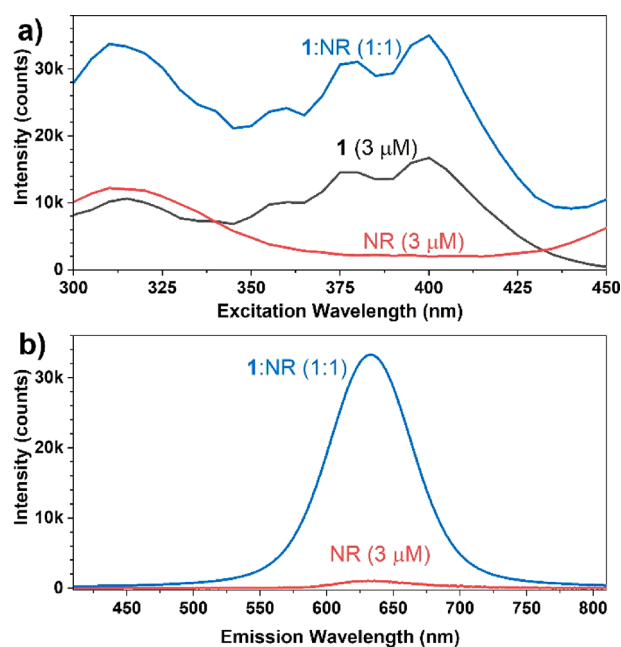


Figure 8. (a) Excitation spectra of 1, NR, and their 1:1 mixture highlighting the excitation contribution of 1 for the NR emission probed at 635 nm and (b) deconvoluted emission spectra of NR* (blue) showing its improved intensity in the presence of the equivalent amount of cage 1 at $\lambda_{\text{ex}} = 400 \text{ nm}$ (for clarity, the NR emission is extracted by using the Voigt deconvolution of the experimental data containing 1; see text and Figure S30). Experimental conditions: $[1] = 3 \mu\text{M}$; $[\text{NR}] = 3 \mu\text{M}$; DMSO solvent.

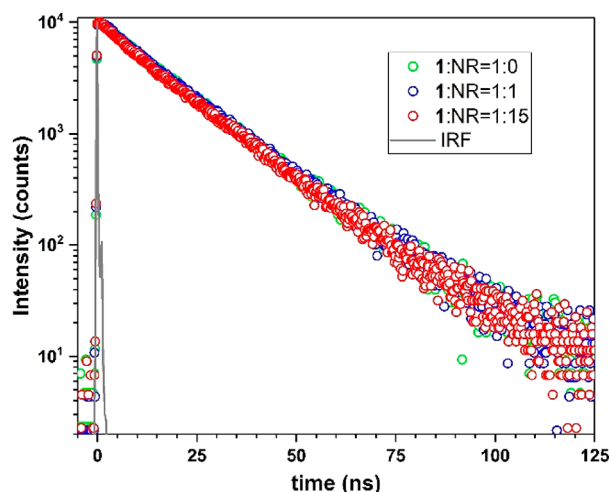


Figure 9. Transient emission decay profiles for the pristine 1 ($3 \mu\text{M}$; green) and in the presence of $3 \mu\text{M}$ NR (blue) and $45 \mu\text{M}$ NR (red) probed at 540 nm in DMSO solvent ($\lambda_{\text{ex}} = 403 \text{ nm}$).

the formation of a possible nonemissive (ground-state) complex between the cages and NR.

To glean into the nature of these cage–NR complexations, we performed a series of experiments. First, emission spectra of the cages in the presence of a different concentration of NR were collected in an emissive titration experiment. The emissive contributions of the cage and NR were deconvoluted through a Voigt profile analysis and used for a Stern–Volmer type analyses (Figure 10; see Figure S33):

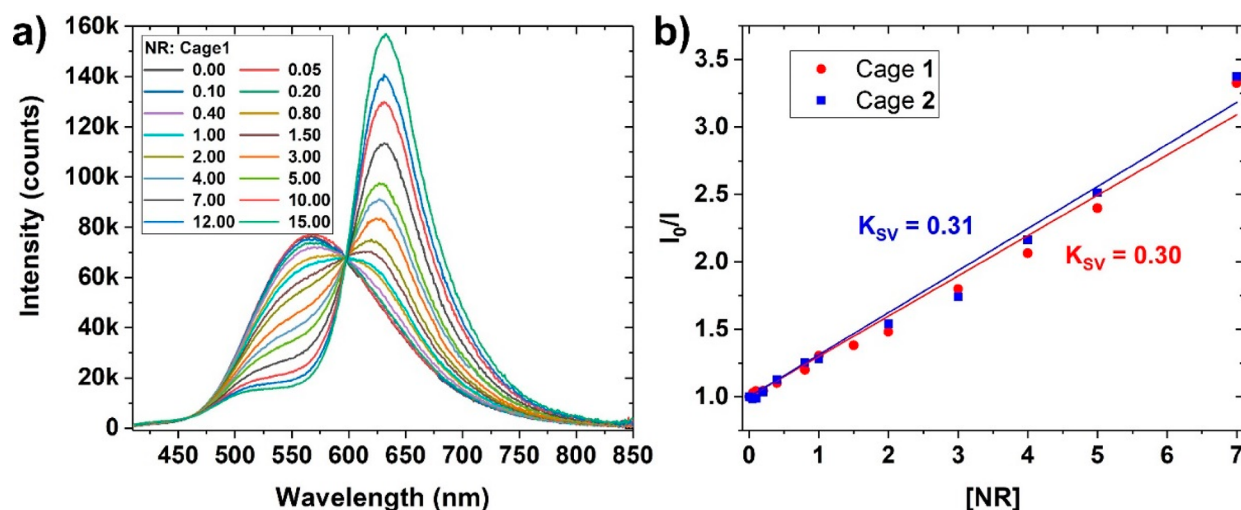


Figure 10. (a) Emissive titration for 3 μM **1** with varying amounts of NR (0–45 μM , $\lambda_{\text{ex}} = 400$ nm; see Figure S34 for similar titration of **2**) (b) The corresponding SV plot of **1** and **2** in the presence of different concentration ratios of NR.

$$\frac{I_0}{I} = 1 + K_s[\text{NR}] \quad (1)$$

where I_0 and I are the emission intensity of cage **1*** in the absence and presence of NR, and the S–V slope K_{SV} is represented by K_s , the association constant of the complexation. Because there is no change in the fluorescence time constant, $I_0/I \neq \tau_0/\tau$ (the $\tau_0/\tau = 1$ in our experiment). Figure 10 highlights that both the cages manifest an identical K_s value of $\sim 0.3 \mu\text{M}^{-1}$, meaning $\sim 3.3 \mu\text{M}$ NR is required to quench half of the emission of 1 μM cage. This is consistent with the ^1H NMR spectra of the NR:1 (or 2) mixture that display essentially nonshifted proton peaks compared to the pristine NR and cages components (Figure S17). Such a weak association suggests that the cage and NR may not have formed any complex in that sense—rather, the NR present within a static “effective sphere” at the moment of cage excitation, which led to a quick quenching of the excited cage before they diffuse apart (Figure 11).^{52,53}

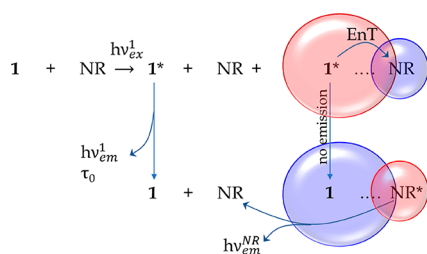


Figure 11. Schematic diagram showing EnT based on an apparent static quenching of **1*** by NR in viscous DMSO medium.

For such a scenario the absorption spectroscopic profiles of the cage should not be altered by the NR: the UV–vis spectra (Figure S35) collected for cage **1** in the presence of 1 and 15 equiv of NR did not display any discernible spectral change (this is also true for the NR component). Furthermore, with the increase in NR concentration, the possibility for NR present within a static effective sphere of a cage molecule will increase and the corresponding I_0/I vs $[\text{NR}]$ Stern–Volmer plot will deviate upward (Figure S36). This apparent static mechanism can be described with a modified S–V equation:

$$\frac{I_0}{Ie^{V[\text{Q}]}} = 1 + K_D[\text{NR}] = \frac{\tau_0}{\tau} \quad (= 1 \text{ in our case and maintained for all } [\text{NR}] \text{ studied}) \quad (2)$$

The parameter V contains the volume information about the active sphere, and K_D is the dynamic S–V constant (different than the K_s discussed in eq 1). Solving for V produces a linear plot with an intercept of one and zero slopes (i.e., no dynamic quenching in place; Figure S37). An active sphere with a radius in the order of tens of nanometers (Note S1 in the Supporting Information) can be extracted from this data. Although a bit overestimated, this large active sphere is clearly referring to a highly diffusion-limited volume in a viscous DMSO solvent ($\eta = 1.99$ cP) where an NR, present adjacent to a cage molecule, cannot diffuse away before quenching (Figure 11). Thus, we can fairly say—even though a dynamic quenching is not observed in this highly viscous medium—the quenching is highly effective, with a rate constant higher than the estimated diffusion-controlled bimolecular rate of ca. $3.7 \times 10^9 \text{ M}^{-1} \text{ s}^{-1}$ (assuming the radius of cage **1** ~ 14 Å and NR ~ 7 Å; Note S2 in Supporting Information). Note that this rate constant accounts for the large size of the cage in highly viscous DMSO solvent, and thus, it is about one order of magnitude slower than common diffusion-controlled bimolecular rates for moderate size fluorophores. What it did not account for is a more realistic picture of much slower diffusion-controlled bimolecular kinetics involving a hexa-cationic cage and its large solvation sphere in a high dielectric solvent; thus, the energy transfer rate $\gtrsim 1 \times 10^9 \text{ s}^{-1}$ can be a good expectation (i.e., corresponding time scale ~ 0.2 – 1 ns). It is important to note that the radiative rate of these cage compounds is much slower ($6.25 \times 10^7 \text{ s}^{-1}$), and thus, any NR present adjacent to the cage (within the active sphere)⁵⁴ will have ample time to efficiently quench its excited state. The underlying EnT that quenches the excited cage also forms NR*, which undergoes radiative recombination.⁵⁵ Given that no dynamic quenching is involved, it is difficult to estimate the EnT efficiency; however, since the NR species adjacent to the cage molecule near-quantitatively quenches the excited cage, we can estimate a $>93\%$ EnT efficiency.⁵⁶ To further probe that improving thermal diffusion will lower the EnT efficiency, we performed the titration at 45 $^\circ\text{C}$, which resulted in a K_s of $0.18 \mu\text{M}^{-1}$

compared to $\sim 0.3 \mu\text{M}^{-1}$ at room temperature (Figure S38). This value indicates that more NR would be required ($5.5 \mu\text{M}$ compared to $\sim 3.3 \mu\text{M}$ at room temperature) to quench half of the emission of the $1 \mu\text{M}$ cage. Experiment at low viscous medium such as CHCl_3 ($\eta = 0.56 \text{ cP}$) can be performed; however, it requires a tedious selection of acceptor chromophore with high spectral overlap and good solubility (for example, our attempt with FITC did not go well due to its poor solubility).

CONCLUSION

In summary, two trigonal prismatic Pt(II) metallacages **1** and **2** were designed and synthesized by using two anthracene–triphenylamine-based tripyridyl ligands as the faces, three dicarboxylates as the pillars, and six 90° Pt(II) acceptors as the linkers. The excited state of the anthracene–triphenylamine-based ligand possesses a stable planar polar quinoidal conformation, which is strongly coupled with the initially generated aromatic excited state. The energy of the polar quinoidal conformer can be tuned by the solvent polarity. Such photophysical behaviors are maintained in their respective cage assemblies which manifest good photon absorptivity ($\geq 2\times$ of the linker) without significant spectral shift and good emission QY with unchanged lifetime. The polar excited state, accessed and stabilized in DMSO solvent, radiatively decays with a longer lifetime (16 ns) than the initially generated aromatic excited state which can be stabilized in CHCl_3 solvent (3 ns). Although not studied here, one of two ligands in these cage assemblies can be expected to attain the planar quinoidal structure where the other ligand remains in its higher energy aromatic conformation and therefore can efficiently tunnel its excited energy to the planar component: in other words, two ligands in the cage can technically work in tandem to emit from the planar component. These features make such cage compounds to be exploited as a superior photosensitizer. With appropriate spectral characteristics, the energy transfer with Nile Red was studied. In a viscous DMSO medium, the diffusion of both the photosensitizer and acceptor is restricted which led to an EnT through an apparent static quenching mechanism, where NR adjacent to the cage (i.e., within an active sphere) efficiently quenches the excited cage. This study opens new design criteria for the fabrication of highly efficient LHSs in the future.

EXPERIMENTAL SECTION

Materials and Methods. All reagents were commercially available and used as supplied without further purification. Deuterated solvents were purchased from Cambridge Isotope Laboratory (Andover, MA). 4-(10-Bromoanthracen-9-yl)pyridine,⁵⁷ (nitrilotris-(benzene-4,1-diyl)triboronic acid,³⁴ and **6**⁵⁸ were prepared according to the literature procedures. Carboxylate ligands **4** and **5** were prepared by neutralization of terephthalic acid with 2 equiv of NaOH. NMR spectra were recorded on a Varian Unity 300, 500, or 600 MHz spectrometers. ^1H and ^{13}C NMR chemical shifts were reported relative to residual solvent signals, and ^{31}P NMR chemical shifts are referenced to an external unlocked sample of 85% H_3PO_4 ($\delta = 0.0$). Mass spectra were recorded on a Micromass Quattro II triple-quadrupole mass spectrometer using electrospray ionization with a MassLynx operating system. The UV–vis experiments were conducted on a Hitachi U-4100 spectrophotometer (absorption).

Steady-state emission and excitation–emission mapping spectra and emission QYs were recorded by using an Edinburgh Instruments FSS spectrofluorometer measured with corresponding solutions in a $1 \times 1 \text{ cm}^2$ quartz cuvette. Temperature-dependent emission spectra

were collected in a quartz capillary tube (ID = 3 mm) in a home-built Dewar cell in the front-face configuration. The absolute quantum yields were measured by using a 150 mm integrating sphere, where respective background spectra were collected by using a cuvette filled with the corresponding solvent. The QY values were calculated with EI F980 software that accounts for the diminished intensity (counts) of the incident beam over the increased intensity (counts) of fluorescence, based on the manually selected wavelength range. Recorded spectra were corrected by using the instrumental correction functions for the excitation light source as well as detector response. Fluorescence lifetime emission decay profiles were recorded by using an Edinburgh Lifespec II picosecond time-correlated single photon counting spectrophotometer equipped with a Hamamatsu H10720-01 detector and a 405 nm picosecond pulsed diode laser as TCSPC source (IRF $\approx 150 \text{ ps}$). An iterative reconvolution procedure with exponential fitting used the EI F980 software to extract lifetime data.

Synthesis of Ligand 3. A 100 mL flask was charged with 4-(10-bromoanthracen-9-yl)pyridine (1.00 g, 3 mmol), (nitrilotris(benzene-4,1-diyl)triboronic acid (226 mg, 0.6 mmol), $\text{Pd}(\text{PPh}_3)_4$ (69.3 mg, 0.06 mmol), Cs_2CO_3 (978 mg, 3 mmol), and toluene/methanol (45 mL/15 mL). The reaction mixture was then heated at 80°C under nitrogen for 48 h with stirring. After cooling to room temperature, the solvent was removed under reduced pressure. The resulting mixture was extracted with ethyl acetate ($3 \times 50 \text{ mL}$). The combined organic layers were washed with brine (100 mL), dried over MgSO_4 , and evaporated to dryness under vacuum. The residue was purified by silica gel chromatography (methanol/ethyl acetate, 10/1) to afford 397 mg of 4-(anthracen-9-yl)pyridine (**3**) as a pale-yellow solid in 58% yield. ^1H NMR (500 MHz, CDCl_3 , 298 K) δ : 8.90 (d, $J = 5.2 \text{ Hz}$, 6H), 7.98 (d, $J = 8.9 \text{ Hz}$, 6H), 7.70 (d, $J = 8.3 \text{ Hz}$, 6H), 7.64 (d, $J = 8.7 \text{ Hz}$, 6H), 7.55 (d, $J = 8.2 \text{ Hz}$, 6H), 7.49 (d, $J = 5.0 \text{ Hz}$, 6H), 7.46 (d, $J = 8.5 \text{ Hz}$, 6H), 7.44–7.40 (m, 6H). ^{13}C NMR (126 MHz, CDCl_3 , 298 K) δ : 150.03, 147.79, 147.15, 137.93, 133.66, 133.21, 132.43, 129.99, 129.17, 127.27, 126.61, 126.14, 125.78, 125.30, 124.26. To compare with the metallacages, ^1H NMR in acetone- d_6 is also shown. ^1H NMR (500 MHz, acetone- d_6 , 298 K) δ : 8.90 (d, $J = 5.8 \text{ Hz}$, 6H), 7.97 (d, $J = 8.0 \text{ Hz}$, 6H), 7.79 (d, $J = 8.5 \text{ Hz}$, 6H), 7.63 (d, $J = 7.8 \text{ Hz}$, 6H), 7.61 (d, $J = 8.3 \text{ Hz}$, 6H), 7.54 (d, $J = 5.9 \text{ Hz}$, 6H), 7.50–7.47 (m, 12H). HRMS (ESI, m/z): calcd for $\text{C}_{75}\text{H}_{49}\text{N}_4$ ($M + \text{H}^+$): 1005.3952; found: 1005.3949.

Self-Assembly of 1. Ligand **3** (2.52 mg, $2.5 \mu\text{mol}$), dicarboxylate ligand **4** (0.79 mg, $3.75 \mu\text{mol}$), and *cis*-(PEt_3)₂Pt(OTf)₂ **6** (5.48 mg, $7.5 \mu\text{mol}$) were mixed in a 2:3:6 molar ratio and dissolved in acetone/water (8.0 mL, 8:2, v/v). The mixture was stirred for 12 h at 35°C and then cooled to room temperature. The solvent was removed by nitrogen flow. Acetone (6.0 mL) was added to the mixture, and the solution was stirred for 12 h at 35°C . After cooling to room temperature, the solution was filtered to remove insoluble materials and the solvent was again removed by nitrogen flow. The solid was dissolved in acetone (1.0 mL) and followed by the addition of 7 mL of diethyl ether. The resulting precipitate was collected by centrifugation to give 7.5 mg of **1** as a pale-yellow solid in 92% yield. ^1H NMR (500 MHz, acetone- d_6 , 298 K) δ : 9.28 (d, $J = 5.1 \text{ Hz}$, 12H), 7.97–7.95 (m, 24H), 7.84 (d, $J = 5.1 \text{ Hz}$, 12H), 7.69–7.67 (m, 12H), 7.59 (d, $J = 8.6 \text{ Hz}$, 24H), 7.43 (d, $J = 8.3 \text{ Hz}$, 24H), 2.23–2.17 (m, 72H), 1.46–1.39 (m, 108H). ^{31}P { ^1H } NMR (acetone- d_6 , 121 MHz, 298 K) δ (ppm): 8.02 (d, $^2J_{\text{P-P}} = 21.4 \text{ Hz}$, ^{195}Pt satellites, $^1J_{\text{Pt-P}} = 3263 \text{ Hz}$), and 2.46 (d, $^2J_{\text{P-P}} = 21.5 \text{ Hz}$, ^{195}Pt satellites, $^1J_{\text{Pt-P}} = 3400 \text{ Hz}$). ESI-TOF-MS: m/z 1347.15 ($[\text{M} - 4\text{OTf}]^{4+}$); found: 1347.20. m/z 1846.86 ($[\text{M} - 3\text{OTf}]^{3+}$); found: 1846.80.

Self-Assembly of 2. Ligand **3** (2.52 mg, $2.5 \mu\text{mol}$), dicarboxylate ligand **5** (1.08 mg, $3.75 \mu\text{mol}$), and *cis*-(PEt_3)₂Pt(OTf)₂ **6** (5.48 mg, $7.5 \mu\text{mol}$) were mixed in a 2:3:6 molar ratio and dissolved in acetone/water (8.0 mL, 8:2, v/v). The mixture was stirred for 12 h at 35°C and then cooled to room temperature. The solvent was removed by nitrogen flow. Acetone (6.0 mL) was added to the mixture, and the solution was stirred for 12 h at 35°C . After cooling to room temperature, the solution was filtered to remove insoluble materials, and the solvent was again removed by nitrogen flow. The solid was dissolved in acetone (1.0 mL) and followed by the addition of 7 mL

of diethyl ether. The resulting precipitate was collected by centrifugation to give 7.8 mg of **2** as a pale-yellow solid in 90% yield. ^1H NMR (500 MHz, acetone- d_6) δ : 9.26 (s, 12H), 8.05 (d, J = 8.3 Hz, 12H), 7.96–7.91 (m, 12H), 7.79–7.73 (m, 36H), 7.65–7.58 (m, 24H), 7.49–7.34 (m, 24H), 2.24–2.19 (m, 72H), 1.49–1.40 (m, 108H). ^{31}P $\{^1\text{H}\}$ NMR (121 MHz, acetone- d_6) δ (ppm): 7.92 (d, $^2J_{\text{P-P}}$ = 21.7 Hz, ^{195}Pt satellites, $^1J_{\text{Pt-P}}$ = 3251 Hz), and 2.70 (d, $^2J_{\text{P-P}}$ = 21.3 Hz, ^{195}Pt satellites, $^1J_{\text{Pt-P}}$ = 3427 Hz). ESI-TOF-MS: m/z 1404.17 ($[\text{M} - 4\text{OTf}]^{3+}$); found: 1404.16. m/z 1921.88 ($[\text{M} - 3\text{OTf}]^{3+}$); found: 1921.81.

Computational Methods. To find the ground-state structures of the host **1** and **2**, the lowest energy conformers of each metallacage components, **3** and **4**, were found by using Spartan 16⁵⁹ conformational search with a MMFF⁶⁰ force field. Then, the lowest energy conformers were combined to build metallacages **1** and **2** and further optimized by using the PM6⁶¹ method in Gaussian09.⁶²

■ ASSOCIATED CONTENT

SI Supporting Information

The Supporting Information is available free of charge via the Internet at. The Supporting Information is available free of charge at <https://pubs.acs.org/doi/10.1021/jacs.0c12853>.

Syntheses and characterization data (NMR, ESI-TOF-MS, fluorescence spectra), including Figures S1–S40; calculation data (PDF)

■ AUTHOR INFORMATION

Corresponding Authors

Yanrong Li – Institute of Chemistry and BioMedical Sciences, School of Chemistry and Chemical Engineering, Nanjing University, Nanjing 210093, China; Department of Chemistry, University of Utah, Salt Lake City, Utah 84112, United States; orcid.org/0000-0001-5180-1965; Email: dg1524042@smail.nju.edu.cn

Pravas Deria – Department of Chemistry and Biochemistry, Southern Illinois University, Carbondale, Illinois 62901, United States; orcid.org/0000-0001-7998-4492; Email: pderia@siu.edu

Peter J. Stang – Department of Chemistry, University of Utah, Salt Lake City, Utah 84112, United States; orcid.org/0000-0002-2307-0576; Email: stang@chem.utah.edu

Authors

Sreehari Surendran Rajasree – Department of Chemistry and Biochemistry, Southern Illinois University, Carbondale, Illinois 62901, United States

Ga Young Lee – Department of Chemistry and Biochemistry, University of California, Los Angeles, Los Angeles, California 90095, United States

Jierui Yu – Department of Chemistry and Biochemistry, Southern Illinois University, Carbondale, Illinois 62901, United States; orcid.org/0000-0001-8422-3583

Jian-Hong Tang – Department of Chemistry, University of Utah, Salt Lake City, Utah 84112, United States; orcid.org/0000-0002-3299-5167

Ruidong Ni – Department of Chemistry, University of South Florida, Tampa, Florida 33620, United States

Guigen Li – Institute of Chemistry and BioMedical Sciences, School of Chemistry and Chemical Engineering, Nanjing University, Nanjing 210093, China; Department of Chemistry and Biochemistry, Texas Tech University, Lubbock, Texas 79409-1061, United States; orcid.org/0000-0002-9312-412X

Kendall N. Houk – Department of Chemistry and Biochemistry, University of California, Los Angeles, Los Angeles, California 90095, United States; orcid.org/0000-0002-8387-5261

Complete contact information is available at: <https://pubs.acs.org/10.1021/jacs.0c12853>

Author Contributions

Y.L. and S.S.R. contributed equally to this work.

Notes

The authors declare no competing financial interest.

■ ACKNOWLEDGMENTS

G.L. thanks the Robert A. Welch Foundation (D-1361, USA) and the National Natural Science Foundation of China (22071102 and 91956110). P.D. acknowledges funding from the U.S. National Science Foundation (NSF CAREER CHE-1944903). Y.L. thanks Z. Yang, Q. Zhang, X. Wang, and B. Shi for discussions and checking the data.

■ REFERENCES

- (1) McDermott, G.; Prince, S. M.; Freer, A. A.; Hawthornthwaite-Lawless, A. M.; Papiz, M. Z.; Cogdell, R. J.; Isaacs, N. W. Crystal structure of an integral membrane light-harvesting complex from photosynthetic bacteria. *Nature* **1995**, *374*, 517–521.
- (2) Ajayaghosh, A.; Praveen, V. K.; Vijayaku-mar, C. Organogels as scaffolds for excitation energy transfer and light harvesting. *Chem. Soc. Rev.* **2008**, *37*, 109–122.
- (3) Frischmann, P. D.; Mahata, K.; Wurthner, F. Powering the future of molecular artificial photosynthesis with light-harvesting metal-losupramolecular dye assemblies. *Chem. Soc. Rev.* **2013**, *42*, 1847–1870.
- (4) Peng, H.-Q.; Niu, L.-Y.; Chen, Y.-Z.; Wu, L.-Z.; Tung, C.-H.; Yang, Q.-Z. Biological Applications of Supramolecular Assemblies Designed for Excitation Energy Transfer. *Chem. Rev.* **2015**, *115*, 7502–7542.
- (5) McCusker, J. K. Electronic structure in the transition metal block and its implications for light harvesting. *Science* **2019**, *363*, 484–488.
- (6) Xiao, T.; Zhong, W.; Zhou, L.; Xu, L.; Sun, X.-Q.; Elmes, R. B. P.; Hu, X.-Y.; Wang, L. Artificial light-harvesting systems fabricated by supramolecular host–guest interactions. *Chin. Chem. Lett.* **2019**, *30*, 31–36.
- (7) Ke, X.-S.; Kim, T.; Lynch, V. M.; Kim, D.; Sessler, J. L. Flattened Calixarene-like Cyclic BODIPY Array: A New Photosynthetic Antenna Model. *J. Am. Chem. Soc.* **2017**, *139*, 13950–13956.
- (8) Guo, S.; Song, Y.; He, Y.; Hu, X.-Y.; Wang, L. Highly Efficient Artificial Light-Harvesting Systems Constructed in Aqueous Solution Based on Supramolecular Self-Assembly. *Angew. Chem., Int. Ed.* **2018**, *57*, 3163–3167.
- (9) Sun, C.-L.; Peng, H.-Q.; Niu, L.-Y.; Chen, Y.-Z.; Wu, L.-Z.; Tung, C.-H.; Yang, Q.-Z. Artificial light-harvesting supramolecular polymeric nanoparticles formed by pillar [5] arene-based host–guest interaction. *Chem. Commun.* **2018**, *54*, 1117–1120.
- (10) Li, C.; Zhang, J.; Zhang, S.; Zhao, Y. Efficient Light-Harvesting Systems with Tunable Emission through Controlled Precipitation in Confined Nanospace. *Angew. Chem., Int. Ed.* **2019**, *58*, 1643–1647.
- (11) Yoshizawa, M.; Klosterman, J. K.; Fujita, M. Functional Molecular Flasks: New Properties and Reactions within Discrete, Self-Assembled Hosts. *Angew. Chem., Int. Ed.* **2009**, *48*, 3418–3438.
- (12) Chakrabarty, R.; Mukherjee, P. S.; Stang, P. J. Supramolecular Coordination: Self-Assembly of Finite Two- and Three-Dimensional Ensembles. *Chem. Rev.* **2011**, *111*, 6810–6918.
- (13) Zhang, D.; Ronson, T. K.; Nitschke, J. R. Functional Capsules via Subcomponent Self-Assembly. *Acc. Chem. Res.* **2018**, *51*, 2423–2436.

- (14) Wu, G.-Y.; Chen, L.-J.; Xu, L.; Zhao, X.-L.; Yang, H.-B. Construction of supramolecular hexagonal metallacycles via coordination-driven self-assembly: Structure, properties and application. *Coord. Chem. Rev.* **2018**, *369*, 39–75.
- (15) Jongkind, L. J.; Caumes, X.; Hartendorp, A. P. T.; Reek, J. N. H. Ligand Template Strategies for Catalyst Encapsulation. *Acc. Chem. Res.* **2018**, *51*, 2115–2128.
- (16) Jansze, S. M.; Severin, K. Clathrochelate Metalloligands in Supramolecular Chemistry and Materials Science. *Acc. Chem. Res.* **2018**, *51*, 2139–2147.
- (17) Hong, C. M.; Bergman, R. G.; Raymond, K. N.; Toste, F. D. Self-Assembled Tetrahedral Hosts as Supramolecular Catalysts. *Acc. Chem. Res.* **2018**, *51*, 2447–2455.
- (18) Sun, Y.; Chen, C.; Stang, P. J. Soft Materials with Diverse Suprastructures via the Self-Assembly of Metal–Organic Complexes. *Acc. Chem. Res.* **2019**, *52*, 802–817.
- (19) Ward, M. D.; Hunter, C. A.; Williams, N. H. Coordination Cages Based on Bis(pyrazolylpyridine) Ligands: Structures, Dynamic Behavior, Guest Binding, and Catalysis. *Acc. Chem. Res.* **2018**, *51*, 2073–2082.
- (20) Zhang, M.; Li, S.; Yan, X.; Zhou, Z.; Saha, M. L.; Wang, Y.-C.; Stang, P. J. Fluorescent metallacycle-cored polymers via covalent linkage and their use as contrast agents for cell imaging. *Proc. Natl. Acad. Sci. U. S. A.* **2016**, *113*, 11100–11105.
- (21) Yu, G.; Cook, T. R.; Li, Y.; Yan, X.; Wu, D.; Shao, L.; Shen, J.; Tang, G.; Huang, F.; Chen, X.; Stang, P. J. Tetraphenylethene-based highly emissive metallacage as a component of theranostic supramolecular nanoparticles. *Proc. Natl. Acad. Sci. U. S. A.* **2016**, *113*, 13720–13725.
- (22) Cai, L.-X.; Li, S.-C.; Yan, D.-N.; Zhou, L.-P.; Guo, F.; Sun, Q.-F. Water-Soluble Redox-Active Cage Hosting Polyoxometalates for Selective Desulfurization Catalysis. *J. Am. Chem. Soc.* **2018**, *140*, 4869–4876.
- (23) Cook, T. R.; Stang, P. J. Recent Developments in the Preparation and Chemistry of Metallacycles and Metallacages via Coordination. *Chem. Rev.* **2015**, *115*, 7001–7045.
- (24) Howlader, P.; Mondal, B.; Purba, P. C.; Zangrando, E.; Mukherjee, P. S. Self-Assembled Pd(II) Barrels as Containers for Transient Merocyanine Form and Reverse Thermochromism of Spiropyran. *J. Am. Chem. Soc.* **2018**, *140*, 7952–7960.
- (25) Yan, X.; Cook, T. R.; Wang, P.; Huang, F.; Stang, P. J. Highly emissive platinum(II) metallacages. *Nat. Chem.* **2015**, *7*, 342–348.
- (26) Zheng, Y.-R.; Zhao, Z.; Wang, M.; Ghosh, K.; Pollock, J. B.; Cook, T. R.; Stang, P. J. A Facile Approach toward Multicomponent Supramolecular Structures: Selective Self-Assembly via Charge Separation. *J. Am. Chem. Soc.* **2010**, *132*, 16873–16882.
- (27) Zhang, M.; Saha, M. L.; Wang, M.; Zhou, Z.; Song, B.; Lu, C.; Yan, X.; Li, X.; Huang, F.; Yin, S.; Stang, P. J. Multicomponent Platinum(II) Cages with Tunable Emission and Amino Acid Sensing. *J. Am. Chem. Soc.* **2017**, *139*, 5067–5074.
- (28) Sun, Y.; Yao, Y.; Wang, H.; Fu, W.; Chen, C.; Saha, M. L.; Zhang, M.; Datta, S.; Zhou, Z.; Yu, H.; Li, X.; Stang, P. J. Self-Assembly of Metallacages into Multidimensional Suprastructures with Tunable Emissions. *J. Am. Chem. Soc.* **2018**, *140*, 12819–12828.
- (29) Sun, Y.; Chen, C.; Liu, J.; Stang, P. J. Recent developments in the construction and applications of platinum-based metallacycles and metallacages via coordination. *Chem. Soc. Rev.* **2020**, *49*, 3889–3919.
- (30) Zhang, Z.; Zhao, Z.; Hou, Y.; Wang, H.; Li, X.; He, G.; Zhang, M. Aqueous Platinum(II)-Cage-Based Light-Harvesting System for Photocatalytic Cross-Coupling Hydrogen Evolution Reaction. *Angew. Chem.* **2019**, *131*, 8954–8958.
- (31) Acharyya, K.; Bhattacharyya, S.; Sepehrpour, H.; Chakraborty, S.; Lu, S.; Shi, B.; Li, X.; Mukherjee, P. S.; Stang, P. J. Self-Assembled Fluorescent Pt(II) Metallacycles as Artificial Light-Harvesting Systems. *J. Am. Chem. Soc.* **2019**, *141*, 14565–14569.
- (32) Endo, A.; Suzuki, K.; Yoshihara, T.; Tobita, S.; Yahiro, M.; Adachi, C. Measurement of photoluminescence efficiency of Ir(III) phenylpyridine derivatives in solution and solid-state films. *Chem. Phys. Lett.* **2008**, *460*, 155–157.
- (33) Katoh, R.; Suzuki, K.; Furube, A.; Kotani, M.; Tokumaru, K. Fluorescence Quantum Yield of Aromatic Hydrocarbon Crystals. *J. Phys. Chem. C* **2009**, *113*, 2961–2965.
- (34) Tang, J.-H.; Sun, Y.; Gong, Z.-L.; Li, Z.-Y.; Zhou, Z.; Wang, H.; Li, X.; Saha, M. L.; Zhong, Y.-W.; Stang, P. J. Temperature-Responsive Fluorescent Organoplatinum(II) Metallacycles. *J. Am. Chem. Soc.* **2018**, *140*, 7723–7729.
- (35) Tang, J.-H.; Ni, R.; He, Y.-Q.; Vanderlinden, R. T.; Li, Y.; Shi, B.; Li, Z.-Y.; Wang, H.; Li, X.; Sun, Y.; Zhong, Y.-W.; Stang, P. J. Metal–Organic Pt(II) Hexagonal-Prism Macrocycles and Their Photophysical Properties. *Inorg. Chem.* **2019**, *58*, 13376–13381.
- (36) Zhang, M.-D.; Shi, Z.-Q.; Chen, M.-D.; Zheng, H.-G. Chiral crystallization and optical properties of three metal complexes based on two non-centrosymmetric tripodal ligands. *Dalton T.* **2015**, *44*, 5818–5825.
- (37) Chang, X.; Zhou, Z.; Shang, C.; Wang, G.; Wang, Z.; Qi, Y.; Li, Z.-Y.; Wang, H.; Cao, L.; Li, X.; Fang, Y.; Stang, P. J. Coordination-Driven Self-Assembled Metallacycles Incorporating Pyrene: Fluorescence Mutability, Tunability, and Aromatic Amine Sensing. *J. Am. Chem. Soc.* **2019**, *141*, 1757–1765.
- (38) Li, S.; Huang, J.; Cook, T. R.; Pollock, J. B.; Kim, H.; Chi, K.-W.; Stang, P. J. Formation of [3]Catenanes from 10 Precursors via Multicomponent Coordination-Driven Self-Assembly of Metallarectangles. *J. Am. Chem. Soc.* **2013**, *135*, 2084–2087.
- (39) Wang, M.; Zheng, Y.-R.; Ghosh, K.; Stang, P. J. Metallosupramolecular Tetragonal Prisms via Multicomponent Coordination-Driven Template-Free Self-Assembly. *J. Am. Chem. Soc.* **2010**, *132*, 6282–6283.
- (40) Zheng, Y.-R.; Lan, W.-J.; Wang, M.; Cook, T. R.; Stang, P. J. Designed Post-Self-Assembly Structural and Functional Modifications of a Truncated Tetrahedron. *J. Am. Chem. Soc.* **2011**, *133*, 17045–17055.
- (41) Wang, M.; Zheng, Y.-R.; Cook, T. R.; Stang, P. J. Construction of Functionalized Metallosupramolecular Tetragonal Prisms via Multicomponent Coordination-Driven Self-Assembly. *Inorg. Chem.* **2011**, *50*, 6107–6113.
- (42) Li, Z.; Ishizuka, H.; Sei, Y.; Akita, M.; Yoshizawa, M. Extended Fluorochromism of Anthracene Trimers with a meta-Substituted Triphenylamine or Triphenylphosphine Core. *Chem. - Asian J.* **2012**, *7*, 1789–1794.
- (43) Zhou, Z.; Hauke, C. E.; Song, B.; Li, X.; Stang, P. J.; Cook, T. R. Understanding the Effects of Coordination and Self-Assembly on an Emissive Phenothiazine. *J. Am. Chem. Soc.* **2019**, *141*, 3717–3722.
- (44) Note: such ligand-to-metal charge transfer type transitions are expected to be highly stabilized with diminished oscillator strength in a polar solvent. Indeed, the TD-DFT computation for a few lowest energy excited states, performed for cages **1** and **2** (Tables S1–S3), suggests that their vertical excitation would involve an electronic transition from anthracene-centered occupied orbitals to node-centered unoccupied orbitals (Figures S39 and S40).
- (45) Sekiguchi, S.; Kondo, K.; Sei, Y.; Akita, M.; Yoshizawa, M. Engineering Stacks of V-Shaped Polyaromatic Compounds with Alkyl Chains for Enhanced Emission in the Solid State. *Angew. Chem., Int. Ed.* **2016**, *55*, 6906–6910.
- (46) Sundstrom, V.; Pullerits, T.; van Grondelle, R. Photosynthetic Light-Harvesting: Reconciling Dynamics and Structure of Purple Bacterial LH2 Reveals Function of Photosynthetic Unit. *J. Phys. Chem. B* **1999**, *103*, 2327–2346.
- (47) Krueger, B. P.; Scholes, G. D.; Fleming, G. R. Calculation of Couplings and Energy-Transfer Pathways between the Pigments of LH2 by the ab Initio Transition Density Cube Method. *J. Phys. Chem. B* **1998**, *102*, 5378–5386.
- (48) Förster, T. Energiewanderung und Fluoreszenz. *Naturwissenschaften* **1946**, *33*, 166–175.
- (49) Son, H.-J.; Jin, S.; Patwardhan, S.; Wezenberg, S. J.; Jeong, N. C.; So, M.; Wilmer, C. E.; Sarjeant, A. A.; Schatz, G. C.; Snurr, R. Q.; Farha, O. K.; Wiederrecht, G. P.; Hupp, J. T. Light-Harvesting and Ultrafast Energy Migration in Porphyrin-Based Metal–Organic Frameworks. *J. Am. Chem. Soc.* **2013**, *135*, 862–869.

(50) Yu, J.; Anderson, R.; Li, X.; Xu, W.; Goswami, S.; Rajasree, S. S.; Maindan, K.; Gomez-Gualdrón, D. A.; Deria, P. Improving Energy Transfer within Metal–Organic Frameworks by Aligning Linker Transition Dipoles along the Framework Axis. *J. Am. Chem. Soc.* **2020**, *142*, 11192–11202.

(51) Note: the heterocyclic N atom of the NR is sterically less accessible, whereas the amine is involved in conjugation with the aromatic core and, therefore, is less likely to coordinate to Pt(II) by replacing the pyridine moieties of the ligand. The stability of the cages in the presence of Nile Red was further probed via ^1H NMR for NR:cage mixtures in acetone (Figure S17), which did not display any shift of proton compared with the each component. No cage dissociation related spectral change was also observed.

(52) *Principles of Fluorescence Spectroscopy*, 3rd ed.; Lakowicz, J. R., Ed.; Springer: p 285.

(53) Eftink, M. R.; Ghiron, C. A. Fluorescence Quenching of Indole and Model Micelle Systems. *J. Phys. Chem.* **1976**, *80*, 486–493.

(54) Note: this slow diffusion rate, estimated above, for a large hexacationic fluorophore and a polar acceptor in viscous medium provides some clues for why the radius of active sphere is so large.

(55) Note: even though the cage is still within the sphere, but due to its higher bandgap, it cannot quench a NR*.

(56) Note: this estimation is based on the tiny residual emission in the presence of large equivalent NR compared to the pristine cage without NR.

(57) Ramsay, W. J.; Szczypiński, F. T.; Weissman, H.; Ronson, T. K.; Smulders, M. M. J.; Rybtchinski, B.; Nitschke, J. R. Designed Enclosure Enables Guest Binding Within the 4200 Å³ Cavity of a Self-Assembled Cube. *Angew. Chem., Int. Ed.* **2015**, *54*, 5636–5640.

(58) Stang, P. J.; Cao, D. H.; Saito, S.; Arif, A. M. Self-Assembly of Cationic, Tetranuclear, Pt(II) and Pd(II) Macrocyclic Squares. x-ray Crystal Structure of [Pt₂+(dppp)(4,4'-bipyridyl).cntdot.2-OSO₂CF₃]₄. *J. Am. Chem. Soc.* **1995**, *117*, 6273–6283.

(59) Hehre, W. J. *Spartan 16*; Wavefunction, Inc.: Irvine, CA, 2016.

(60) Halgren, T. A. Merck molecular force field. 1. Basis, form, scope, parameterization, and performance of MMFF94. *J. Comput. Chem.* **1996**, *17*, 490–519.

(61) Stewart, J. J. P. Optimization of parameters for semiempirical methods V: Modification of NDDO approximations and application to 70 elements. *J. Mol. Model.* **2007**, *13*, 1173–1213.

(62) Frisch, M. J.; Trucks, G. W.; Schlegel, H. B.; Scuseria, G. E.; Robb, M. A.; Cheeseman, J. R.; Scalmani, G.; Barone, V.; Mennucci, B.; Petersson, G. A.; Nakatsuji, H.; Caricato, M.; Li, X.; Hratchian, H. P.; Izmaylov, A. F.; Bloino, J.; Zheng, G.; Sonnenberg, J. L.; Hada, M.; Ehara, M.; Toyota, K.; Fukuda, R.; Hasegawa, J.; Ishida, M.; Nakajima, T.; Honda, Y.; Kitao, O.; Nakai, H.; Vreven, T.; Montgomery, J. A.; Peralta, J. E.; Ogliaro, F.; Bearpark, M.; Heyd, J. J.; Brothers, E.; Kudin, K. N.; Staroverov, V. N.; Kobayashi, R.; Normand, J.; Raghavachari, K.; Rendell, A.; Burant, J. C.; Iyengar, S. S.; Tomasi, J.; Cossi, M.; Rega, N.; Millam, J. M.; Klene, M.; Knox, J. E.; Cross, J. B.; Bakken, V.; Adamo, C.; Jaramillo, J.; Gomperts, R.; Stratmann, R. E.; Yazyev, O.; Austin, A. J.; Cammi, R.; Pomelli, C.; Ochterski, J. W.; Martin, R. L.; Morokuma, K.; Zakrzewski, V. G.; Voth, G. A.; Salvador, P.; Dannenberg, J. J.; Dapprich, S.; Daniels, A. D.; Farkas, J. B.; Foresman, J. B.; Ortiz, J. V.; Cioslowski, J.; Fox, D. J. *Gaussian 09*; Gaussian Inc.: Wallingford, CT, 2009.